Chiral phonons in sixfold chiral CrSi$_2$: Raman spectroscopy and first-principles calculations

Gakuto Kusuno [1,*], Shingo Kisanuki,[2] Yusuke Kousaka,[2] Yoshihiko Togawa [2,3] and Takuya Satoh [1,3,†]

[1]*Department of Physics, Institute of Science Tokyo, Meguro-ku, Tokyo 152-8551, Japan*

[2]*Department of Physics and Electronics, Osaka Metropolitan University, Sakai, Osaka 599-8531, Japan*

[3]*Quantum Research Center for Chirality, Institute for Molecular Science, Okazaki, Aichi 444-8585, Japan*

Chiral phonons have been identified in several chiral crystals, primarily in crystals with trigonal symmetry and threefold screw axes. In this study, chiral phonons in CrSi$_2$, a chiral crystal with a sixfold helical structure, were investigated. Circularly polarized Raman spectroscopy revealed a subtle splitting of doubly degenerate E_2 phonon modes between cross-circular polarization configurations. These observations, supported by first-principles phonon calculations, indicate the presence of chiral phonons in CrSi$_2$, expanding the scope of materials that exhibit chiral vibrational modes beyond the conventional trigonal class.

I. INTRODUCTION

In recent years, rotational atomic motions in crystals have attracted significant attention in the field of condensed-matter physics. Phonons endowed with angular momentum arising from such rotations have been theoretically predicted and experimentally observed in connection with diverse phenomena [1], including the phonon Zeeman effect [2–6], the phonon Hall effect [7,8], and their topological characteristics [9,10]. Although these phonons have been investigated extensively in two-dimensional materials [11,12], chiral crystals offer distinct opportunities, such as mechanical rotation along an axis parallel to the temperature gradient [13] and chirality-induced selectivity of phonon polarizations [14,15]. In particular, phonons that carry finite angular momentum and propagate with a finite wave vector along the rotation axis are referred to as "chiral phonons" that satisfy the definition of true chirality [16,17].

Observation of chiral phonons in chiral materials has been achieved using circularly polarized Raman spectroscopy in α-HgS [18], Te [19], and α-quartz [20] and also by resonant inelastic x-ray scattering in α-quartz [21]. These materials share the same threefold helical structure, with space groups limited to $P3_221$ (left-handed) and $P3_121$ (right-handed). In such chiral materials, the energy splitting of chiral phonons with opposite angular momenta in reciprocal space makes them particularly suitable for exciting chiral phonons [22]. However, experimental evidence of chiral phonons in other types of chiral structures has been lacking.

Sixfold helical structures are of particular interest because of their similarities to trigonal counterparts. For instance, certain transition metal disilicides (MSi$_2$, $M =$ V, Nb, Ta) crystallize in sixfold helical structures [23,24]. These materials exhibit chirality-related phenomena, such as chirality-induced

spin selectivity with long-range propagation [25–27], as well as characteristic electronic band structures [28–31].

While these chiral disilicides are metallic, less conductive materials are more suitable for investigation by Raman scattering. In this study, the focus was on the semiconductor disilicide CrSi$_2$, which possesses a sixfold helical axis with left-handed $P6_422$ (L-CrSi$_2$) and right-handed $P6_222$ (R-CrSi$_2$) enantiomorphs. Circularly polarized Raman spectroscopy was applied to CrSi$_2$ crystals. The results demonstrate that the direction of energy splitting in doubly degenerate phonon modes can be predicted based on the phonon crystal- (or pseudo-)angular momentum (CAM), analogous to the case of trigonal chiral materials. Moreover, it was found that each split peak corresponded to a pair of chiral phonons carrying opposite angular momenta and opposite CAM.

II. METHODS

A. Sample preparation

CrSi$_2$ is a nonmagnetic semiconductor with a bandgap of 0.35 eV [32–35]. It crystallizes into a C40 structure with a sixfold screw axis [36]. Its chirality arises from double helical chains formed by Si−Si and Si−Cr bonds. The two enantiomeric structures are related to each other by either spatial inversion or mirror symmetry, as illustrated in Fig. 1(a).

Crystals of CrSi$_2$ were synthesized using two methods: the laser-diode-heated floating zone (LDFZ) method [37] and the chemical vapor transport (CVT) method [38,39]. In the LDFZ method, the handedness of the synthesized crystals can be controlled by using a seed rod with a predetermined handedness. In contrast, the CVT method does not provide selective control over crystal handedness.

Two enantiomeric crystals of CrSi$_2$ were synthesized using the LDFZ method. The first crystal, grown from a left-handed seed, was identified as left-handed (L-CrSi$_2$) by absolute structure analysis using single-crystal x-ray diffraction (XRD). The Flack parameter [40] was determined to be

---

*Contact author: kusuno.g.2b7e@m.isct.ac.jp

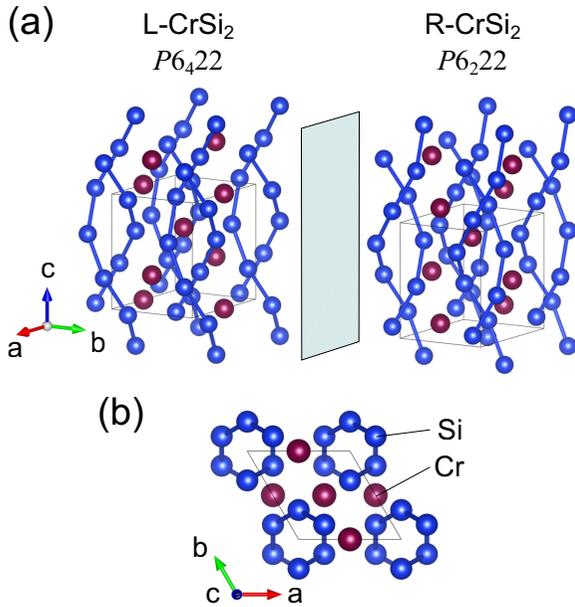†Contact author: satoh@phys.sci.isct.ac.jp

FIG. 1. Crystal structures of CrSi$_2$: (a) L- and R-CrSi$_2$, which are mirror images of each other, and (b) sixfold crystal structure viewed along the c axis.
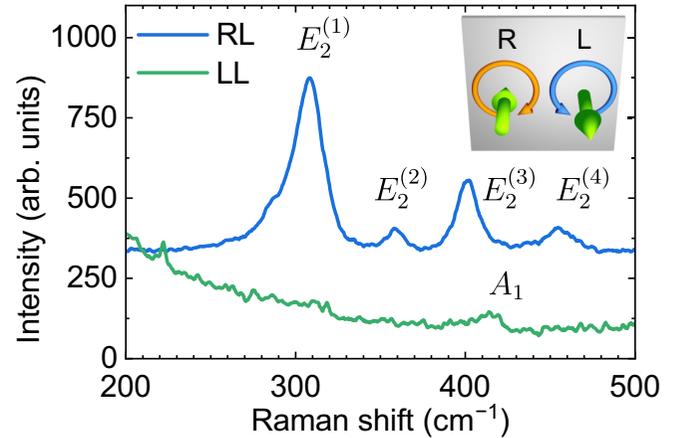

FIG. 2. Stokes Raman spectra and phonon mode assignments for the L-CrSi$_2$ crystal: vertical offsets have been added for clarity. The inset shows the RL configuration. Here, R and L are defined as the direction of polarization rotation in the sample plane, irrespective of the propagation direction.

-0.114 ± 0.134 (with the uncertainty corresponding to one standard deviation: σ), confirming its handedness. The uniform handedness throughout the entire crystal, approximately 3 mm in size, was further verified by circularly polarized resonant x-ray diffraction [41]. The second crystal was grown using a right-handed seed rod and identified as right-handed (R-CrSi$_2$) based on XRD measurements, with a Flack parameter of 0.098 ± 0.116.

Additional crystals were synthesized by the CVT method in a temperature gradient using iodine as the transport agent. The CVT-grown crystals typically exhibited hexagonal shapes with sizes of approximately 200 μm. Sample No. 1 was identified as left-handed by XRD, with a Flack parameter of -0.002 ± 0.142. For Sample No. 2, however, the large uncertainty ($\sigma > 0.25$) prevented a reliable determination of its handedness.

B. Circularly polarized Raman spectroscopy

All Raman measurements were conducted at room temperature (295 K) using an excitation wavelength of 785 nm in the backscattering geometry perpendicular to the c-plane of the crystal [Fig. 1(b)]. The Raman measurement system was custom-built and equipped with a spectrometer (Princeton Instruments, SpectraPro 2500i) and a CCD array sensor (Hamamatsu Photonics, S11501-1007S). Two polarizers and a quarter-wave plate allow full control of the incident and scattered light polarizations. For example, RL denotes the right-circularly polarized incident light and left-circularly polarized scattered light (see the inset of Fig. 2). The cross-circular polarization (LR and RL) configurations are particularly useful for detecting chiral phonons, because the phonon CAM excited in these configurations is well separated. Because of the energy splitting of doubly degenerate phonon modes with different CAM at finite wave vectors along the Γ–A (helical

chain) direction of the Brillouin zone, chiral phonons can be detected as small differences in Raman shift between the cross-circular polarization configurations [9,18–20].

The unit cell of CrSi$_2$ contains three Cr atoms and six Si atoms, yielding 27 phonon modes. Among these, the Raman-active modes are classified as $\Gamma = A_1 + 4E_1 + 4E_2$. The doubly degenerate E_1 modes can be observed under oblique incidence relative to the c axis of the crystal. However, because the Raman measurements were performed under normal incidence along the c axis, the E_1 modes were suppressed. The other doubly degenerate modes, E_2, were observed in the cross-circular polarization configurations, whereas the nondegenerate A_1 modes appeared in the parallel-circular polarization (LL and RR) configurations. The rotational motions of the four E_2 phonon modes are shown in the Supplemental Material Movie [42].

C. First-principles calculations

First-principles phonon calculations were performed using density functional perturbation theory, as implemented in the ABINIT software package [43–45], to verify the experimental results. All calculations employed the local-density approximation for the exchange-correlation functional formulated by Perdew and Wang [46]. The projector augmented-wave method [47,48] was used for pseudopotentials, and a plane-wave energy cutoff of 25 Ha was applied. The Brillouin zone was sampled using a $4 \times 4 \times 4$ Monkhorst–Pack k-point grid [49], shifted to include the Γ point. Phonon dispersion relations were calculated on a $4 \times 4 \times 4$ q-point grid.

III. EXPERIMENTAL RESULTS AND DISCUSSION

A. Raman measurements of LDFZ-grown crystals

Figure 2 shows the Stokes Raman spectra of the L-CrSi$_2$ crystal grown by the LDFZ method, together with the corresponding phonon mode assignments. The E_2 and A_1 modes were observed in the cross- and parallel-circular polarization

TABLE I. Raman shifts (cm^{-1}) of observed and calculated phonon modes.

	$E_1^{(3)}$	$E_2^{(1)}$	$E_1^{(4)}$	$E_2^{(2)}$	$E_2^{(3)}$	A_1	$E_2^{(4)}$
Exp.	292	308	-	359	401	412	456
Calc.	316	339	370	377	423	436	484
Ref. [50] (Exp.)	301	307–311	357	354	399	413	-
Ref. [50] (Calc.)	282	311	336	338	388	403	448

(RL and LL) configurations, respectively. The observed Raman shifts, obtained by fitting the spectra with Voigt functions, and the mode assignments were consistent with our first-principles calculations and Raman selection rules (see Appendix A) as well as with reported values [50], as summarized in Table I.

The $E_2^{(1)}$ mode can be fitted with two Voigt functions. Under the ideal backscattering geometry along the c axis, the E_1 modes are symmetry-forbidden. However, slight misalignment from the ideal geometry can weakly relax the selection rules, leading to small contributions from E_1 modes. We attribute the observed two-peak structure of the $E_2^{(1)}$ mode to such weak E_1-mode contributions, whose frequencies are close to the frequency of the $E_2^{(1)}$ mode (see Table I). These contributions are extrinsic and negligible compared with the intrinsic chiral splitting discussed in this work, and are therefore excluded from the subsequent peak-fitting analyses.

Stokes spectra of the L-CrSi$_2$ crystal obtained in the cross-circular polarization (LR and RL) configurations are shown in Figs. 3(a)–3(d). All four E_2 phonon modes exhibited small but discernible differences in Raman shift between the LR and RL spectra. The RL configuration exhibited higher Raman shifts than the LR configuration for the $E_2^{(1)}$ and $E_2^{(3)}$ modes, whereas the opposite trend was observed for the $E_2^{(2)}$ and $E_2^{(4)}$ modes. Moreover, the Stokes spectra of the R-CrSi$_2$ crystal exhibited energy splittings in the opposite direction [Figs. 3(e)–3(h)], which is consistent with the opposite crystal handedness.

To extract the splitting widths quantitatively, all Raman peaks were fitted using a Voigt profile, given by the convolution of a Gaussian and a Lorentzian function. The Gaussian width was fixed to 2.7 cm^{-1} to represent the instrumental
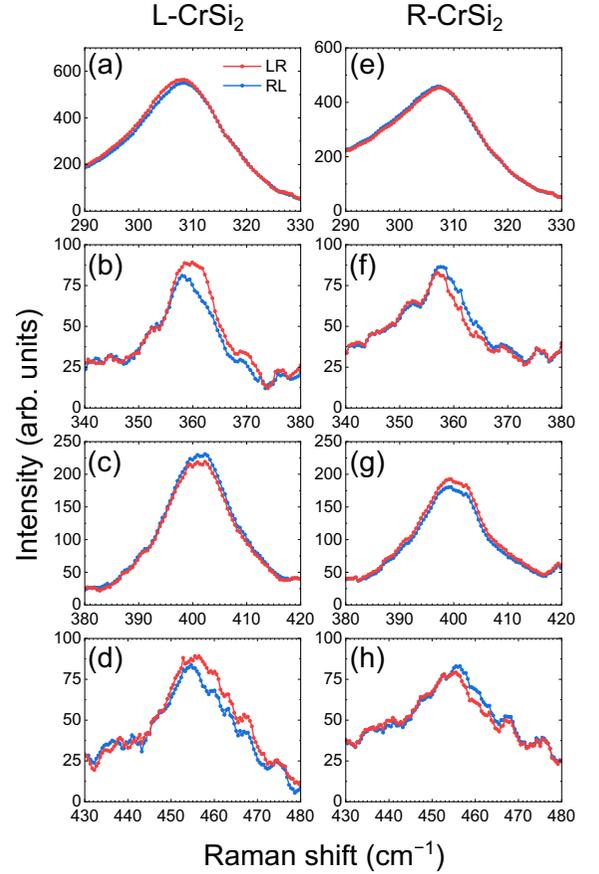

FIG. 3. Stokes spectra of the four E_2 modes of (a)–(d) L- and (e–h) R-CrSi$_2$ in cross-circular polarization configurations: (a), (e) $E_2^{(1)}$, (b), (f) $E_2^{(2)}$, (c), (g) $E_2^{(3)}$, and (d), (h) $E_2^{(4)}$ peaks, showing polarization-dependent energy splittings.

response, while the Lorentzian component accounts for the intrinsic phonon linewidth. The uncertainties of the splitting widths listed in Tables II and III correspond to the standard errors obtained from these Voigt-function fits. The observed splittings are larger than the fitting uncertainties and are well resolved within the signal-to-noise ratio of the measured spectra, demonstrating that the splittings are statistically significant despite their small magnitude.

TABLE II. Frequencies and energy splittings of chiral phonons in L-CrSi$_2$, measured using circularly polarized Raman spectroscopy and compared with first-principles calculations. The errors in the peak splittings were estimated from the uncertainties of the Voigt-function fits.

Peak	Experiment			Calculation			
	Polarization	Frequency (cm^{-1})	Splitting (cm^{-1})	CAM	AM	Frequency (cm^{-1})	Splitting (cm^{-1})
$E_2^{(1)}$	LR	306.7	$+0.3 \pm 0.1$	-2	$-$	338.8	$+0.1$
	RL	307.0		$+2$	$+$	338.9	
$E_2^{(2)}$	LR	359.2	-1.0 ± 0.2	-2	$+$	377.4	-0.8
	RL	358.2		$+2$	$-$	376.5	
$E_2^{(3)}$	LR	401.1	$+0.1 \pm 0.1$	-2	$+$	422.6	$+0.5$
	RL	401.2		$+2$	$-$	423.1	
$E_2^{(4)}$	LR	456.1	-1.0 ± 0.3	-2	$+$	484.2	-0.7
	RL	455.2		$+2$	$-$	483.5	

TABLE III. Frequencies and energy splittings of chiral phonons in CVT-grown $CrSi_2$ crystals, measured in the cross-circular polarization configurations. The errors in the peak splittings were estimated from the uncertainties of the Voigt-function fits.

Peak	Polarization	Sample No. 1		Sample No. 2	
		Frequency (cm^{-1})	Splitting (cm^{-1})	Frequency (cm^{-1})	Splitting (cm^{-1})
$E_2^{(1)}$	LR	313.6	$+0.3 \pm 0.1$	312.6	-0.4 ± 0.1
	RL	314.0		312.2	
$E_2^{(2)}$	LR	359.9	-1.4 ± 0.1	357.3	$+1.1 \pm 0.1$
	RL	358.4		358.4	
$E_2^{(3)}$	LR	401.2	$+0.2 \pm 0.1$	400.2	-0.4 ± 0.1
	RL	401.5		399.9	
$E_2^{(4)}$	LR	456.5	-1.0 ± 0.3	454.6	$+0.9 \pm 0.2$
	RL	455.5		455.5	

The observed splitting magnitudes ($\leqslant 1 \, cm^{-1}$) in $CrSi_2$ are comparable to those reported in trigonal chiral crystals such as α-HgS, Te, and α-quartz under similar experimental conditions. These splittings originate from the same underlying physical mechanism, namely, symmetry-allowed lifting of degeneracy for chiral phonons at finite wave vector. We emphasize that the physical origin and magnitude of the splittings are governed by three main factors: (i) the lattice structure, (ii) the excitation wavelength, and (iii) the phonon dispersion properties. For factors (i) and (ii), the size of the Brillouin zone along the crystal c axis and the excitation wavelength determine the phonon wave vector involved in Raman scattering. A longer c axis and a shorter excitation wavelength lead to larger phonon wave vectors with respect to the size of the Brillouin zone, and thus larger splittings, since the splitting is approximately proportional to the phonon wave vector. For factor (iii), different E_2 phonon modes possess different degrees of chirality, which are reflected in the group velocities along the c axis. These group velocities determine how rapidly the splitting increases with increasing phonon wave vector. From a symmetry viewpoint, the linear-in-q splitting of chiral phonons is a generic consequence of lattice chirality. Recent theoretical work has shown that such a splitting can be described by an effective Hamiltonian with a pseudoscalar coupling constant, which is allowed only in chiral crystals and is determined by the lattice structure and force constants [51].

B. Calculations of phonon CAM

The splittings of the E_2 modes can be understood from the conservation of CAM. The concept of CAM is analogous to that of the crystal momentum, in that it is a discrete and conserved quantity determined by crystal symmetry. CAM is a symmetry-based quantum number defined by the eigenvalue of the rotational (or screw) symmetry operator acting on the phonon eigendisplacement, and it characterizes how the collective atomic motion transforms under crystal rotational symmetries. In the left-handed $P6_422$ structure, the CAM of phonons m is defined as [11,52–54]

$$\left\{ C_6^+ \left| \frac{4\mathbf{c}}{6} \right\} \mathbf{u}_j(\mathbf{q}) = \exp\left[-\frac{2\pi i}{6}\left(m + \frac{4\mathbf{q} \cdot \mathbf{c}}{2\pi} \right) \right] \mathbf{u}_j(\mathbf{q}), \quad (1)$$

where $\mathbf{c}$ is the primitive lattice vector along the c axis of the crystal, and $\mathbf{u}_j(\mathbf{q})$ represents the phonon eigendisplacement of the j-th branch at wave vector $\mathbf{q}$. The CAM of phonons in hexagonal crystals takes integer values $m = 0, \pm1, \pm2, 3$.

The CAM was numerically calculated for phonons in $CrSi_2$ along the Γ–A line using Eq. (1), based on the results of the first-principles calculations. The results for L-$CrSi_2$ are shown in Fig. 4(a). Each doubly degenerate mode at the Γ point clearly splits into two non-degenerate modes with opposite CAM values at finite wave vectors along the Γ–A direction. The E_2 modes correspond to CAM values of $m = \pm2$ (colored red and blue).

The polarization selection rules, or equivalently, the conservation of CAM in the Raman process [55], lead to the following condition:

$$\sigma_i - \sigma_s \equiv \pm m \quad (\text{mod } 6), \quad (2)$$

where the plus (minus) sign corresponds to the Stokes (anti-Stokes) process, and $\sigma_{i(s)} = \pm1$ denotes the CAM of the incident (scattered) circularly polarized light. The schematic illustration of the conservation of CAM is shown in Fig. 5. Thus, in the cross-circular polarization configurations, only
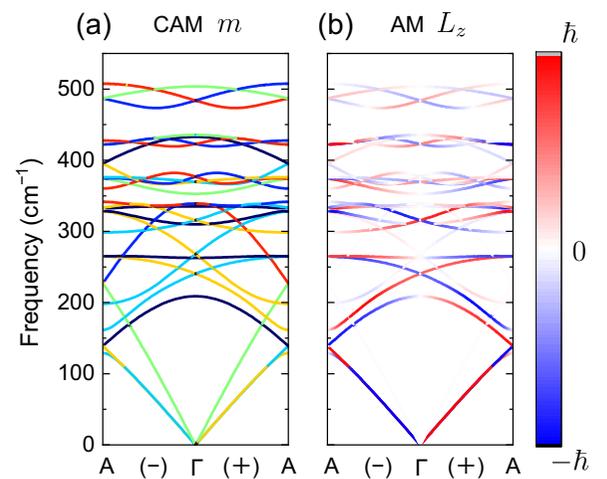

FIG. 4. (a) CAM m and (b) the z component of the angular momentum L_z for phonons in L-$CrSi_2$: the CAM values $m = -2, -1, 0, +1, +2,$ and 3 are shown in blue, sky blue, green, yellow, red, and black, respectively.
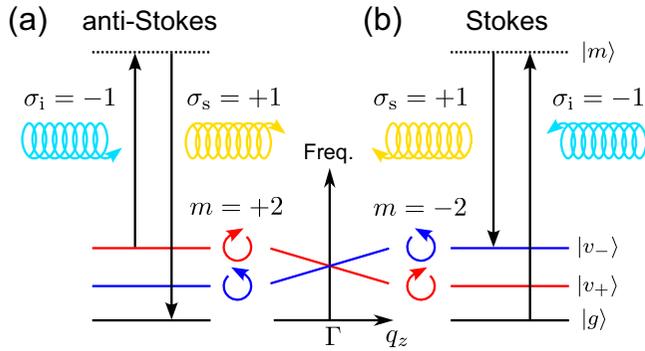
FIG. 5. Schematic illustration of Raman selection rules: (a) anti-Stokes and (b) Stokes processes. $|g\rangle$ denotes the ground state, while $|m\rangle$ represents an intermediate state involved in the Raman transitions and $|v_{+(-)}\rangle$ represents an excited state with CAM $m = \pm 2$ phonons. In this schematic, the incident and scattered photons carry CAM $\sigma_i = -1$ and $\sigma_s = +1$, respectively (LR configuration), resulting in $m = -2$ for the Stokes process and $m = +2$ for the anti-Stokes process.

E_2 phonons with $m = \pm 2$ can be excited. Specifically, the $^1E_2$ phonon ($m = -2$) contributes to the LR configuration ($\sigma_i = -1$, $\sigma_s = +1$), while the $^2E_2$ phonon ($m = +2$) contributes to the RL configuration ($\sigma_i = +1$, $\sigma_s = -1$) in the Stokes process.

In Raman scattering, phonons possess a small but finite wave vector because of the conservation of crystal momentum. In the Stokes process of the present case, the phonon wave vector was approximately 1% of the Brillouin zone size. At positive wave vectors corresponding to the Stokes process, phonons with CAM of $m = +2$ exhibited higher frequencies for the $E_2^{(1)}$ and $E_2^{(3)}$ modes but lower frequencies for the $E_2^{(2)}$ and $E_2^{(4)}$ modes. These calculated energy splittings are consistent with the experimental results, as listed in Table II.

In addition, the sign of the CAM in R-CrSi₂ was opposite to that in L-CrSi₂, as shown in Appendix B. These results demonstrate that the observed splittings of the E_2 phonon modes originate from CAM conservation. At the same time, they indicate that the handedness of a CrSi₂ crystal can be identified from the direction of the splittings observed in Raman scattering. Note that the handedness of the LDFZ-grown crystals determined by Raman measurements was fully consistent with that determined by XRD.

C. Raman measurements of CVT-grown crystals

For completeness, we also measured two CVT-grown crystals, which exhibited sharper Raman lines than the LDFZ-grown samples (Appendix C). Stokes and anti-Stokes spectra of Sample No. 1, identified as L-CrSi₂ by XRD measurements, obtained in the cross-circular polarization configurations are provided in Figs. 6(a)–6(h). All four E_2 phonon modes showed clear differences in Raman shift between the LR and RL spectra. The direction of the splittings was consistent with that of the L-CrSi₂ grown by the LDFZ method. In contrast, the anti-Stokes spectra exhibited splittings in the opposite direction to the Stokes spectra, as expected from the
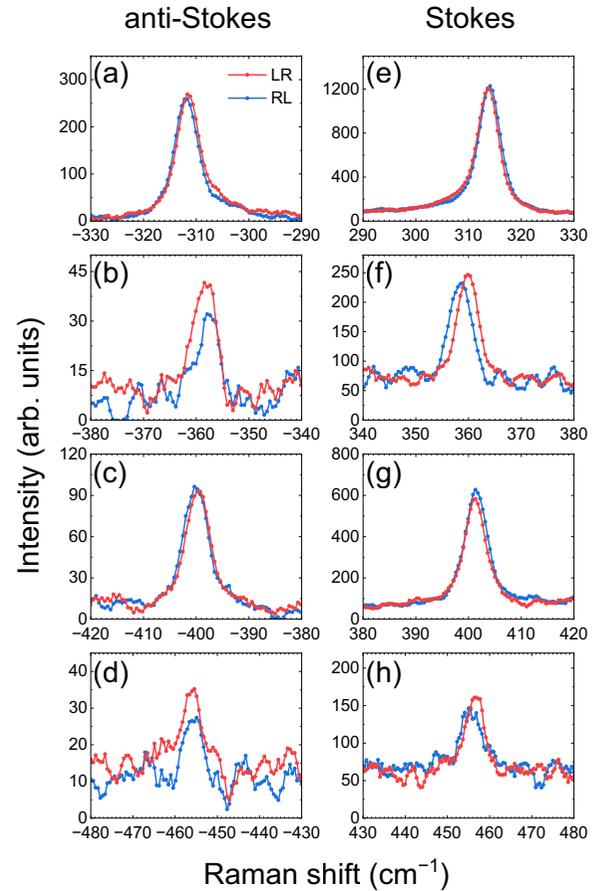

FIG. 6. (a)–(d) Anti-Stokes and (e)–(h) Stokes spectra of the four E_2 modes of Sample No. 1 in cross-circular polarization configurations: (a), (e) $E_2^{(1)}$, (b), (f) $E_2^{(2)}$, (c), (g) $E_2^{(3)}$, and (d), (h) $E_2^{(4)}$ peaks, showing polarization-dependent energy splittings.

reversal of the CAM at negative wave vectors [Fig. 4(a)]. These results further confirm that the observed E_2 phonon splittings strictly follow the selection rules derived from CAM conservation in L-CrSi₂, consistent with the handedness determined by XRD.

Similar splittings of the E_2 modes were also observed in Sample No. 2 [Figs. 7(a)–7(h)]. Importantly, the relation between the LR and RL spectra was consistent with the R-CrSi₂ case summarized in Table III. Thus, the handedness of Sample No. 2, which could not be determined by XRD, can be identified as right-handed by Raman spectroscopy.

D. CAM and angular momentum of phonons

At small but finite wave vector **q**, the lifting of degeneracy allows phonon modes with opposite CAM to split in energy, and the corresponding branches acquire opposite angular momentum. Importantly, CAM and phonon angular momentum are closely related but fundamentally distinct quantities [53,54,56]: the former classifies phonons according to the crystal symmetry, whereas the latter measures the real-space atomic rotation.

The transformation properties of phonons for the crystal symmetry are associated with the irreducible representations
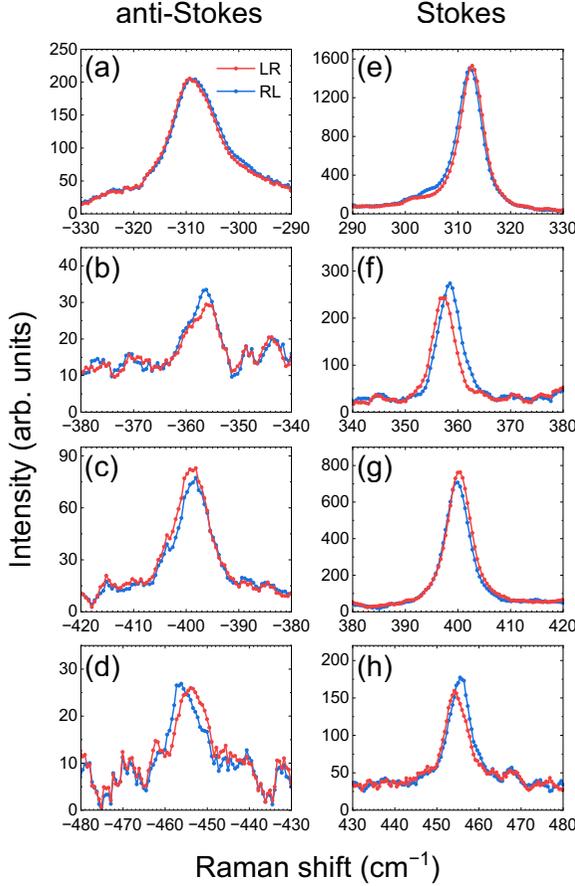
FIG. 7. (a)–(d) Anti-Stokes and (e)–(h) Stokes spectra of the four E_2 modes of Sample No. 2 in cross-circular polarization configurations: (a), (e) $E_2^{(1)}$, (b), (f) $E_2^{(2)}$, (c), (g) $E_2^{(3)}$, and (d), (h) $E_2^{(4)}$ peaks, showing polarization-dependent energy splittings.

of the point group 6 (C_6). As listed in Table IV, each phonon CAM can be directly related to the irreducible representation of the corresponding vibrational mode.

In contrast, the phonon angular momentum originates from the microscopic rotational motion of individual atoms and quantifies the actual mechanical rotation associated with a phonon mode. While CAM is a discrete quantum number that remains constant within a given phonon branch, angular momentum is a continuous quantity that depends on the phonon wave vector **q**. We calculated the phonon angular momentum (Appendix D for details) to verify whether the phonons ob-

TABLE IV. Character table of the point group 6 (C_6) and corresponding CAM m: here, $\omega = \exp(2\pi i/3)$.

Irreps.	E	C_6^+	C_3^+	C_2	C_3^-	C_6^-	CAM
A	1	1	1	1	1	1	0
B	1	-1	1	-1	1	-1	3
$^1E_2$	1	ω	ω^2	1	ω	ω^2	-2
$^2E_2$	1	ω^2	ω	1	ω^2	ω	$+2$
$^2E_1$	1	$-\omega^2$	ω	-1	ω^2	$-\omega$	-1
$^1E_1$	1	$-\omega$	ω^2	-1	ω	$-\omega^2$	$+1$

served in the Raman spectra correspond to chiral phonons. As shown in Fig. 4(b), the E_2 modes exhibited finite angular momenta along their wave vectors. Therefore, the E_2 phonons observed in the cross-circular polarization configurations can be identified as chiral phonons [18].

IV. CONCLUSION

In summary, circularly polarized Raman measurements were performed on the sixfold chiral semiconductor CrSi$_2$. Under normal incidence along the crystal c axis, energy splittings between the two cross-circular polarization configurations were observed in four E_2 phonon modes. These splittings are consistent with the conservation of phonon CAM. First-principles calculations of phonon angular momentum further confirmed that the observed Raman features originate from chiral phonons. The results establish circularly polarized Raman scattering as a powerful probe of chiral phonons and crystal handedness in hexagonal chiral systems, expanding the exploration beyond trigonal materials. Moreover, the splitting of doubly degenerate E_1 or E_2 modes at the Γ point into nondegenerate branches suggests a potential route to exploring topological phonon properties.

DATA AVAILABILITY

The data that support the findings of this article are not publicly available upon publication because it is not technically feasible and/or the cost of preparing, depositing, and hosting the data would be prohibitive within the terms of this research project. The data are available from the authors upon reasonable request.

APPENDIX A: RAMAN SELECTION RULES

1. Derivation of Raman tensors

The Stokes intensity of Raman scattering is proportional to $I \propto |\mathbf{e}_s^\dagger R \mathbf{e}_i|^2$, where $\mathbf{e}_{i(s)}$ denotes the polarization vector of the incident (scattered) light, and R is the Raman tensor. The selection rules are determined by the form of R, which in turn is dictated by the crystal symmetry.

Because the phonon wave vector involved in Raman scattering is small compared with the size of the Brillouin zone, Raman tensors are usually derived from the point group at the

Γ point. However, for finite $\mathbf{q}$, which plays a crucial role in the present case, the symmetry of the phonons and their Raman tensors is governed by the little co-group (the subgroup of the crystal point group that leaves $\mathbf{q}$ invariant).

For the present case of the hexagonal point group 622 (D_6), with the phonon wave vector along the c axis, the relevant symmetry operations reduce to those of the point group 6 (C_6). The corresponding character table is listed in Table II of the main text. Raman tensors adapted to the irreducible representations of point group 6 can be obtained using the projection operator, defined as [57]

$$P_{ij}^r = \frac{d_r}{g} \sum_{R \in G} D_{ij}^{r*}(R) R, \tag{A1}$$

where R denotes a symmetry operation of the group G, g is the order of the group, d_r is the dimension of the irreducible representation r, and $D^r(R)$ is its representation matrix. Applying this operator to a trial matrix yields the Raman tensors for

$$R^A = \begin{pmatrix} a & 0 & 0 \\ 0 & a & 0 \\ 0 & 0 & b \end{pmatrix}, \tag{A2}$$

$$R^{1E_2} = c\begin{pmatrix} 1 & i & 0 \\ i & -1 & 0 \\ 0 & 0 & 0 \end{pmatrix}, \quad R^{2E_2} = d\begin{pmatrix} 1 & -i & 0 \\ -i & -1 & 0 \\ 0 & 0 & 0 \end{pmatrix}. \tag{A3}$$

Here, only the symmetric components are shown. The superscripts of the Raman tensors indicate the phonon modes excited in the Stokes process.

2. Selection rules for the circular polarization configurations

Circular polarization vectors are defined as $\mathbf{e}_L = (1/\sqrt{2}, -i/\sqrt{2}, 0)^\top$ and $\mathbf{e}_R = (1/\sqrt{2}, i/\sqrt{2}, 0)^\top$. Using these definitions, the Raman scattering intensities of Stokes light for the A and E_2 modes can be evaluated as

$$I_{\text{parallel}}^A \propto a^2, \quad I_{\text{cross}}^A = 0, \tag{A4}$$

for the A mode, and

$$I_{\text{LR}}^{1E_2} \propto c^2, \quad I_{\text{RL}}^{1E_2} = I_{\text{parallel}}^{1E_2} = 0, \tag{A5}$$

$$I_{\text{RL}}^{2E_2} \propto d^2, \quad I_{\text{LR}}^{2E_2} = I_{\text{parallel}}^{2E_2} = 0, \tag{A6}$$

for the E_2 modes. Thus, the A mode appears only in the parallel-circular polarization configurations, the $^1E_2$ ($m = -2$) mode only in the LR configuration, and the $^2E_2$ ($m = +2$) mode only in the RL configuration. The obtained selection rules are consistent with the conservation law of CAM.

Formally, the intensities of anti-Stokes light can be obtained by replacing the Raman tensors as $R \to R^*$, since the Stokes and anti-Stokes processes are related by time-reversal symmetry in the limit of zero-phonon frequency. Thus, the intensities can be expressed as

$$I_{\text{parallel,AS}}^A \propto a^2, \quad I_{\text{cross,AS}}^A = 0, \tag{A7}$$

$$I_{\text{LR,AS}}^{2E_2} \propto d^2, \quad I_{\text{RL,AS}}^{1E_2} = I_{\text{parallel}}^{1E_2} = 0, \tag{A8}$$

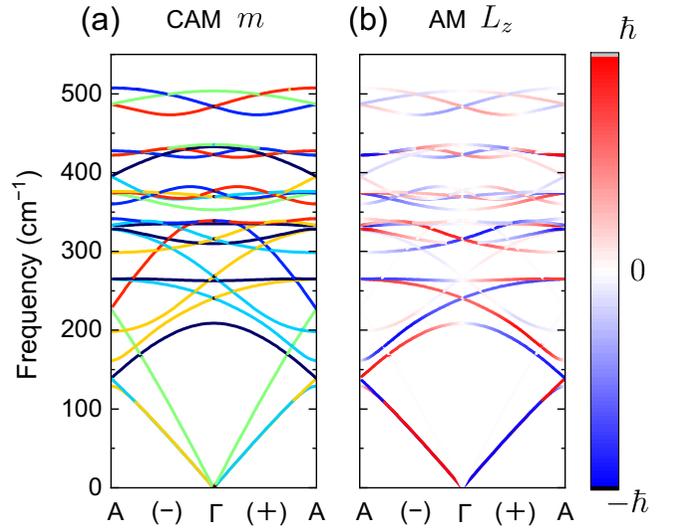$$I_{\text{RL,AS}}^{1E_2} \propto c^2, \quad I_{\text{LR,AS}}^{2E_2} = I_{\text{parallel}}^{2E_2} = 0, \tag{A9}$$

FIG. 8. (a) CAM m and (b) the z component of the angular momentum L_z for phonons in R-CrSi₂: the CAM values $m = -2, -1, 0, +1, +2$, and 3 are shown in blue, sky blue, green, yellow, red, and black, respectively.

indicating that the $^1E_2$ ($m = -2$) modes contribute only to the RL configuration, whereas the $^2E_2$ ($m = +2$) modes contribute only to the LR configuration. Therefore, the conservation law of CAM is preserved in the anti-Stokes process as well.

APPENDIX B: CALCULATION OF PHONONS IN THE RIGHT-HANDED STRUCTURE

In the right-handed $P6_222$ structure, the CAM of the phonons m is defined as [11,52–54]

$$\left\{ C_6^+ \Big| \frac{2\mathbf{c}}{6} \right\} \mathbf{u}_j(\mathbf{q}) = \exp\left[-\frac{2\pi i}{6}\left(m + \frac{2\mathbf{q} \cdot \mathbf{c}}{2\pi} \right) \right] \mathbf{u}_j(\mathbf{q}). \tag{B1}$$

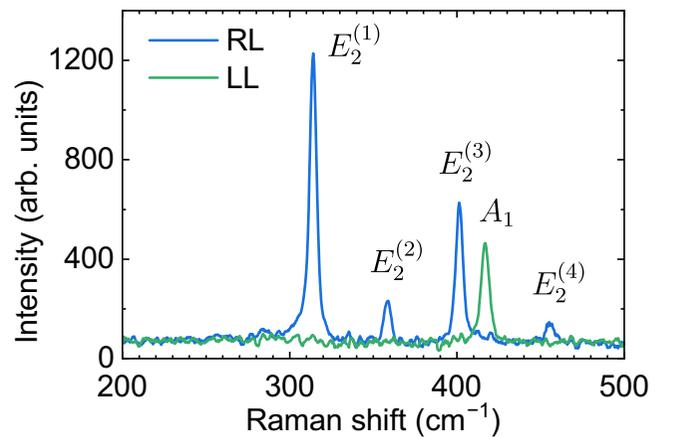Figures 8(a) and 8(b) show the calculated results for the CAM and the phonon angular momentum in R-CrSi₂. The

FIG. 9. Phonon mode assignments for Sample No. 1 grown by the CVT method.

signs of both quantities are reversed compared with those of the L-CrSi$_2$, which is consistent with the opposite crystal chirality.

APPENDIX C: MODE ASSIGNMENTS OF THE CHEMICAL VAPOR TRANSPORT CRYSTAL

Figure 9 shows the phonon mode assignments of Sample No. 1. Compared with the LDFZ-grown crystals discussed in the main text, the CVT-grown crystal exhibited sharper Raman lines, indicating higher crystallinity.

APPENDIX D: CALCULATIONS OF PHONON ANGULAR MOMENTUM

The phonon angular momentum is calculated using the following expression [58]:

$$\mathbf{L}_j(\mathbf{q}) = \hbar \boldsymbol{\epsilon}_j^\dagger(\mathbf{q}) \mathbf{M} \boldsymbol{\epsilon}_j(\mathbf{q}), \quad \text{(D1)}$$

where $\boldsymbol{\epsilon}_j(\mathbf{q})$ is the normalized eigenvector of the dynamical matrix. For the z component, the matrix $\mathbf{M}$ is given by

$$M_z = I_{N \times N} \otimes \begin{pmatrix} 0 & -i & 0 \\ i & 0 & 0 \\ 0 & 0 & 0 \end{pmatrix}. \quad \text{(D2)}$$

[1] T. Wang, H. Sun, X. Li, and L. Zhang, Chiral phonons: Prediction, verification, and application, Nano Lett. **24**, 4311 (2024).

[2] D. M. Juraschek and N. A. Spaldin, Orbital magnetic moments of phonons, Phys. Rev. Mater. **3**, 064405 (2019).

[3] D. M. Juraschek, T. Neuman, and P. Narang, Giant effective magnetic fields from optically driven chiral phonons in 4f paramagnets, Phys. Rev. Res. **4**, 013129 (2022).

[4] J. Luo, T. Lin, J. Zhang, X. Chen, E. R. Blackert, R. Xu, B. I. Yakobson, and H. Zhu, Large effective magnetic fields from chiral phonons in rare-earth halides, Science **382**, 698 (2023).

[5] D. Lujan, J. Choe, S. Chaudhary, G. Ye, C. Nnokwe, M. Rodriguez-Vega, J. He, F. Y. Gao, T. N. Nunley, E. Baldini, J. Zhou, G. A. Fiete, R. He, and X. Li, Spin–orbit exciton–induced phonon chirality in a quantum magnet, Proc. Natl. Acad. Sci. U.S.A. **121**, e2304360121 (2024).

[6] M. Che, J. Liang, Y. Cui, H. Li, B. Lu, W. Sang, X. Li, X. Dong, L. Zhao, S. Zhang, T. Sun, W. Jiang, E. Liu, F. Jin, T. Zhang, and L. Yang, Magnetic order induced chiral phonons in a ferromagnetic Weyl semimetal, Phys. Rev. Lett. **134**, 196906 (2025).

[7] G. Grissonnanche, S. Thériault, A. Gourgout, M.-E. Boulanger, E. Lefrançois, A. Ataei, F. Laliberté, M. Dion, J.-S. Zhou, S. Pyon, T. Takayama, H. Takagi, N. Doiron-Leyraud, and L. Taillefer, Chiral phonons in the pseudogap phase of cuprates, Nat. Phys. **16**, 1108 (2020).

[8] X. Li, B. Fauqué, Z. Zhu, and K. Behnia, Phonon thermal Hall effect in strontium titanate, Phys. Rev. Lett. **124**, 105901 (2020).

[9] T. Zhang, Z. Huang, Z. Pan, L. Du, G. Zhang, and S. Murakami, Weyl phonons in chiral crystals, Nano Lett. **23**, 7561 (2023).

[10] T. Zhang, Y. Liu, H. Miao, and S. Murakami, New advances in phonons: From band topology to quasiparticle chirality, arXiv:2505.06179.

[11] L. Zhang and Q. Niu, Chiral phonons at high-symmetry points in monolayer hexagonal lattices, Phys. Rev. Lett. **115**, 115502 (2015).

[12] H. Zhu, J. Yi, M.-Y. Li, J. Xiao, L. Zhang, C.-W. Yang, R. A. Kaindl, L.-J. Li, Y. Wang, and X. Zhang, Observation of chiral phonons, Science **359**, 579 (2018).

[13] M. Hamada, E. Minamitani, M. Hirayama, and S. Murakami, Phonon angular momentum induced by the temperature gradient, Phys. Rev. Lett. **121**, 175301 (2018).

[14] H. Chen, W. Wu, J. Zhu, Z. Yang, W. Gong, W. Gao, S. A. Yang, and L. Zhang, Chiral phonon diode effect in chiral crystals, Nano Lett. **22**, 1688 (2022).

[15] K. Ohe, H. Shishido, M. Kato, S. Utsumi, H. Matsuura, and Y. Togawa, Chirality-induced selectivity of phonon angular momenta in chiral quartz crystals, Phys. Rev. Lett. **132**, 056302 (2024).

[16] L. D. Barron, Symmetry and molecular chirality, Chem. Soc. Rev. **15**, 189 (1986).

[17] D. M. Juraschek, R. M. Geilhufe, H. Zhu, M. Basini, P. Baum, A. Baydin, S. Chaudhary, M. Fechner, B. Flebus, G. Grissonnanche, A. I. Kirilyuk, M. Lemeshko, S. F. Maehrlein, M. Mignolet, S. Murakami, Q. Niu, U. Nowak, C. P. Romao, H. Rostami, T. Satoh, *et al.*, Chiral phonons, Nat. Phys. **21**, 1532 (2025).

[18] K. Ishito, H. Mao, Y. Kousaka, Y. Togawa, S. Iwasaki, T. Zhang, S. Murakami, J. Kishine, and T. Satoh, Truly chiral phonons in α-HgS, Nat. Phys. **19**, 35 (2023).

[19] K. Ishito, H. Mao, K. Kobayashi, Y. Kousaka, Y. Togawa, H. Kusunose, J. Kishine, and T. Satoh, Chiral phonons: Circularly polarized Raman spectroscopy and *ab initio* calculations in a chiral crystal tellurium, Chirality **35**, 338 (2023).

[20] E. Oishi, Y. Fujii, and A. Koreeda, Selective observation of enantiomeric chiral phonons in α-quartz, Phys. Rev. B **109**, 104306 (2024).

[21] H. Ueda, M. García-Fernández, S. Agrestini, C. P. Romao, J. Van Den Brink, N. A. Spaldin, K.-J. Zhou, and U. Staub, Chiral phonons in quartz probed by x-rays, Nature (London) **618**, 946 (2023).

[22] H. Ishizuka and M. Sato, Nonlinear optical response of truly chiral phonons: Light-induced phonon angular momentum, Peltier effect, and orbital current, arXiv:2505.05313.

[23] O. Chaix-Pluchery, J. Bossy, H. Schober, U. Gottlieb, O. Laborde, and R. Madar, Lattice dynamics of transition metal disilicides, Microelectron. Eng. **37-38**, 551 (1997).

[24] S. Fujio, K. Tanaka, and H. Inui, Formation probability for enantiomorphic crystals (with the space groups of $P6_222$ and $P6_422$) in transition-metal disilicides with the C40 structure as determined by convergent-beam electron diffraction, Intermetallics **15**, 245 (2007).

[25] K. Shiota, A. Inui, Y. Hosaka, R. Amano, Y. Ōnuki, M. Hedo, T. Nakama, D. Hirobe, J. I. Ohe, J. I. Kishine, H. M. Yamamoto, H. Shishido, and Y. Togawa, Chirality-induced spin polarization over macroscopic distances in chiral disilicide crystals, Phys. Rev. Lett. **127**, 126602 (2021).

[26] H. Shishido, R. Sakai, Y. Hosaka, and Y. Togawa, Detection of chirality-induced spin polarization over millimeters in

polycrystalline bulk samples of chiral disilicides NbSi$_2$ and TaSi$_2$, Appl. Phys. Lett. **119**, 182403 (2021).

[27] A. Roy, F. T. Cerasoli, A. Jayaraj, K. Tenzin, M. B. Nardelli, and J. Sławińska, Long-range current-induced spin accumulation in chiral crystals, npj Comput. Mater. **8**, 243 (2022).

[28] H. Tsutsumi, Y. Miura, H. Harima, F. Honda, and Y. Ōnuki, Split Fermi surface properties of VSi$_2$ without mirror Planes in the chiral crystal structure, J. Phys. Soc. Jpn. **82**, 094604 (2013).

[29] Y. Ōnuki, A. Nakamura, T. Uejo, A. Teruya, M. Hedo, T. Nakama, F. Honda, and H. Harima, Chiral-structure-driven split Fermi surface properties in TaSi$_2$, NbSi$_2$, and VSi$_2$, J. Phys. Soc. Jpn. **83**, 061018 (2014).

[30] C. Zhang, T. Shishidou, R. Amano, K. Miyamoto, T. Sayo, C. Shimada, Y. Kousaka, M. Weinert, Y. Togawa, and T. Okuda, Spiral band structure hidden in the bulk chiral crystal NbSi$_2$, Phys. Rev. B **108**, 235164 (2023).

[31] I. Mahraj and A. Ptok, Phonon Weyl points and chiral edge modes with unconventional Fermi arcs in NbSi$_2$, Phys. Rev. B **112**, 075401 (2025).

[32] M. C. Bost and J. E. Mahan, An investigation of the optical constants and band gap of chromium disilicide, J. Appl. Phys. **63**, 839 (1988).

[33] L. F. Mattheiss, Electronic structure of CrSi$_2$ and related refractory disilicides, Phys. Rev. B **43**, 12549 (1991).

[34] V. Bellani, G. Guizzetti, F. Marabelli, A. Piaggi, A. Borghesi, F. Nava, V. N. Antonov, Vl. N. Antonov, O. Jepsen, O. K. Andersen, and V. V. Nemoshkalenko, Theory and experiment on the optical properties of CrSi$_2$, Phys. Rev. B **46**, 9380 (1992).

[35] S. Chen, Y. Chen, W. Yan, S. Zhou, X. Qin, W. Xiong, and L. Liu, Electronic and magnetic properties of Bulk and monolayer CrSi$_2$: A first-principle study, Appl. Sci. **8**, 1885 (2018).

[36] L. F. Mattheiss, Calculated structural properties of CrSi$_2$, MoSi$_2$, and WSi$_2$, Phys. Rev. B **45**, 3252 (1992).

[37] Y. Kousaka, T. Sayo, S. Iwasaki, R. Saki, C. Shimada, H. Shishido, and Y. Togawa, Chirality-selected crystal growth and spin polarization over centimeters of transition metal disilicide crystals, Jpn. J. Appl. Phys. **62**, 015506 (2023).

[38] M. Binnewies, R. Glaum, M. Schmidt, and P. Schmidt, *Chemical Vapor Transport Reactions* (Walter de Gruyter, Berlin, 2012).

[39] J. R. Szczech, A. L. Schmitt, M. J. Bierman, and S. Jin, Single-crystal semiconducting chromium disilicide nanowires synthesized via chemical vapor transport, Chem. Mater. **19**, 3238 (2007).

[40] H. D. Flack, On enantiomorph-polarity estimation, Acta Crystallogr. A **39**, 876 (1983).

[41] Y. Tanaka, T. Takeuchi, S. W. Lovesey, K. S. Knight, A. Chainani, Y. Takata, M. Oura, Y. Senba, H. Ohashi, and S. Shin, Right handed or left handed? Forbidden x-ray diffraction reveals chirality, Phys. Rev. Lett. **100**, 145502 (2008).

[42] See Supplemental Material at http://link.aps.org/supplemental/10.1103/6zdg-1mpt for animations of all E_2 phonons.

[43] X. Gonze, B. Amadon, G. Antonius, F. Arnardi, L. Baguet, J.-M. Beuken, J. Bieder, F. Bottin, J. Bouchet, E. Bousquet, N. Brouwer, F. Bruneval, G. Brunin, T. Cavignac, J.-B. Charraud, W. Chen, M. Côté, S. Cottenier, J. Denier, G. Geneste, *et al.*, The Abinit project: Impact, environment and recent developments, Comput. Phys. Commun. **248**, 107042 (2020).

[44] X. Gonze, First-principles responses of solids to atomic displacements and homogeneous electric fields: Implementation of a conjugate-gradient algorithm, Phys. Rev. B **55**, 10337 (1997).

[45] X. Gonze and C. Lee, Dynamical matrices, Born effective charges, dielectric permittivity tensors, and interatomic force constants from density-functional perturbation theory, Phys. Rev. B **55**, 10355 (1997).

[46] J. P. Perdew and Y. Wang, Accurate and simple analytic representation of the electron-gas correlation energy, Phys. Rev. B **45**, 13244 (1992).

[47] P. E. Blöchl, Projector augmented-wave method, Phys. Rev. B **50**, 17953 (1994).

[48] M. Torrent, F. Jollet, F. Bottin, G. Zérah, and X. Gonze, Implementation of the projector augmented-wave method in the ABINIT code: Application to the study of iron under pressure, Comput. Mater. Sci. **42**, 337 (2008).

[49] H. J. Monkhorst and J. D. Pack, Special points for Brillouin-zone integrations, Phys. Rev. B **13**, 5188 (1976).

[50] P. Hermet, M. Khalil, R. Viennois, M. Beaudhuin, D. Bourgogne, and D. Ravot, Revisited phonon assignment and electro-mechanical properties of chromium disilicide, RSC Adv. **5**, 19106 (2015).

[51] H. Tsunetsugu and H. Kusunose, Chiral phonons in a cubic lattice, J. Phys. Soc. Jpn. **95**, 013601 (2026).

[52] T. Zhang and S. Murakami, Chiral phonons and pseudoangular momentum in nonsymmorphic systems, Phys. Rev. Res. **4**, L012024 (2022).

[53] A. Kato and J. Kishine, Note on angular momentum of phonons in chiral crystals, J. Phys. Soc. Jpn. **92**, 075002 (2023).

[54] T. Tateishi, A. Kato, and J. Kishine, Electron–chiral phonon coupling, crystal angular momentum, and phonon chirality, J. Phys. Soc. Jpn. **94**, 053601 (2025).

[55] Y. Tatsumi, T. Kaneko, and R. Saito, Conservation law of angular momentum in helicity-dependent Raman and Rayleigh scattering, Phys. Rev. B **97**, 195444 (2018).

[56] S. Zhang, Z. Huang, M. Du, T. Ying, L. Du, and T. Zhang, Comprehensive study of phonon chirality under symmetry constraints, Phys. Rev. B **113**, 024302 (2026).

[57] M. S. Dresselhaus, G. Dresselhaus, and A. Jorio, *Group theory: Application to the Physics of Condensed Matter* (Springer, Berline, 2007).

[58] L. Zhang and Q. Niu, Angular momentum of phonons and the Einstein–de Haas effect, Phys. Rev. Lett. **112**, 085503 (2014).